



## Application of a perfectly matched layer in seismic wavefield simulation with an irregular free surface

Haiqiang Lan<sup>1</sup>, Jingyi Chen<sup>1\*</sup>, Zhongjie Zhang<sup>2</sup>, Youshan Liu<sup>2</sup>, Jianguo Zhao<sup>3</sup> and Ruiqi Shi<sup>3</sup>

<sup>1</sup>Department of Geosciences, The University of Tulsa, Tulsa, OK, 74104, USA, <sup>2</sup>State Key Laboratory of Lithospheric Evolution, Institute of Geology and Geophysics, Chinese Academy of Sciences, Beijing, 100029, China, and <sup>3</sup>College of Geophysics and Information Engineering, China University of Petroleum, Beijing, 102249, China

Received April 2014, revision accepted January 2015

### ABSTRACT

Recently, an effective and powerful approach for simulating seismic wave propagation in elastic media with an irregular free surface was proposed. However, in previous studies, researchers used the periodic condition and/or sponge boundary condition to attenuate artificial reflections at boundaries of a computational domain. As demonstrated in many literatures, either the periodic condition or sponge boundary condition is simple but much less effective than the well-known perfectly matched layer boundary condition. In view of this, we intend to introduce a perfectly matched layer to simulate seismic wavefields in unbounded models with an irregular free surface. We first incorporate a perfectly matched layer into wave equations formulated in a frequency domain in Cartesian coordinates. We then transform them back into a time domain through inverse Fourier transformation. Afterwards, we use a boundary-conforming grid and map a rectangular grid onto a curved one, which allows us to transform the equations and free surface boundary conditions from Cartesian coordinates to curvilinear coordinates. As numerical examples show, if free surface boundary conditions are imposed at the top border of a model, then it should also be incorporated into the perfectly matched layer imposed at the top-left and top-right corners of a 2D model where the free surface boundary conditions and perfectly matched layer encounter; otherwise, reflections will occur at the intersections of the free surface and the perfectly matched layer, which is confirmed in this paper. So, by replacing normal second derivatives in wave equations in curvilinear coordinates with free surface boundary conditions, we successfully implement the free surface boundary conditions into the perfectly matched layer at the top-left and top-right corners of a 2D model at the surface. A number of numerical examples show that the perfectly matched layer constructed in this study is effective in simulating wave propagation in unbounded media and the algorithm for implementation of the perfectly matched layer and free surface boundary conditions is stable for long-time wavefield simulation on models with an irregular free surface.

**Key words:** Perfectly matched layer, Irregular free surface, Finite-difference, Seismic wavefield.

\*E-mail: jingyi-chen@utulsa.edu

## INTRODUCTION

The numerical modelling of seismic wave propagation in a medium with irregular topography is beneficial to interpret seismic data acquired in mountainous areas (Sanchez-Sesma, Bravo and Herreir 1985). In the last three decades, several finite-difference methods have been proposed to simulate seismic wave propagation in models with irregular topography (Wong 1982; Fornberg 1988; Jih, McLaughlin and Der 1988; Hestholm and Ruud 1994, 1998; Zhang and Chen 2006; Lombard *et al.* 2008; Rao and Wang 2013). One of the most effective and powerful approaches was proposed by Appelo and Petersson (2009). They constructed a stable discretization of an irregular surface in curvilinear coordinate systems and proved that the strengths of the proposed method were its ease of implementation, efficiency and geometric flexibility (Appelo and Petersson 2009). Recently, Lan and Zhang (2011a, 2012) extended this scheme to model seismic wavefields in anisotropic and fractured media.

In order to model seismic wave propagation in unbounded media, energy needs to be absorbed at the artificial boundaries of the computational domain. Appelo and Petersson (2009) imposed periodic conditions at the boundaries of their models. The periodic boundary is rather simple but far from satisfactory; apparent reflections can be observed in the snapshots of seismic wavefields. In Lan and Zhang's simulations (2011a, 2012), they used a sponge boundary condition (Cerjan *et al.* 1985), which works well if the sponge layer is thick enough. In the last four decades, a variety of absorbing boundary conditions have been developed to suppress the artificial reflections, such as the one-way wave equation (Engquist and Majda 1977; Mur 1981), sponge boundary conditions (Cerjan *et al.* 1985; Tian *et al.* 2008), paraxial boundary conditions (Clayton and Engquist 1977; Yang *et al.* 2003) and continued fraction absorbing boundary conditions (Guddati and Lim 2006). However, Collino and Tsogka (2001) pointed out that all these methods still show relatively strong spurious reflections at grazing incidence.

Berenger (1994) proposed the so-called Perfectly Matched Layer (PML) technique, which is remarkable for generating no reflections theoretically at the interface between the inner medium and the artificial absorbing medium. This method has proven to be very efficient and has gained a lot of attention since it was proposed (Chew and Liu 1996; Roden *et al.* 2000; Collino and Tsogka 2001; Zeng and Liu 2001; Komatitsch and Martin 2007; Martin and Komatitsch *et al.* 2009). Recently, many researchers have extended the

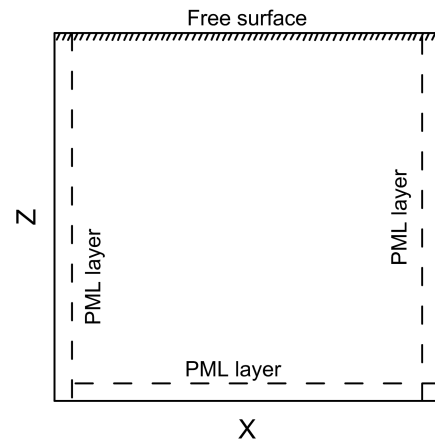
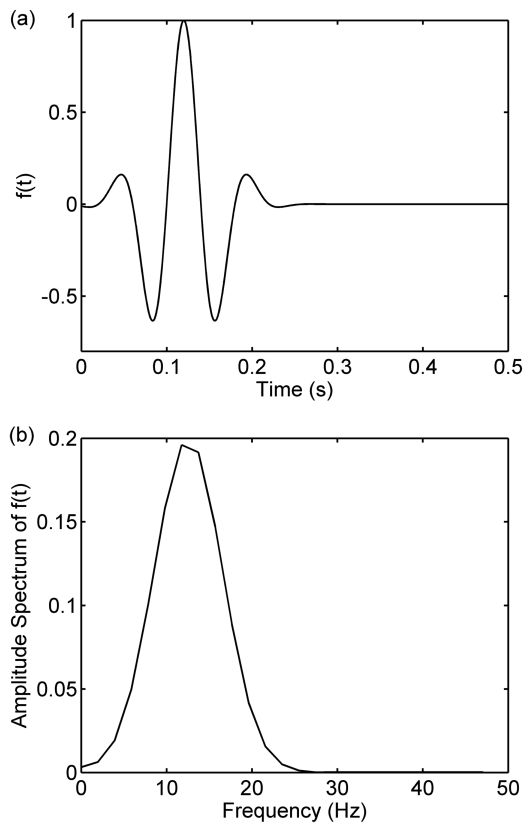
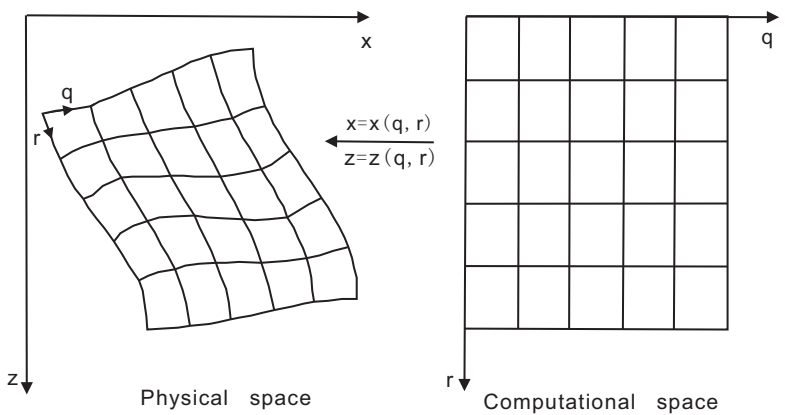


Figure 1 Free surface and perfectly matched layer boundary conditions imposed at the boundaries of a 2D model.

PML from Cartesian coordinates to cylindrical and spherical coordinates, or even more general curvilinear coordinates (Collino and Monk 1998; Teixeira and Chew 2000; Zheng and Huang 2002; Kantartzis 2003). However, no free surface boundary condition (FSBC) was involved in their studies. As free surface always exists at the real surface of the earth and is often accompanied by undulating topography (Jih *et al.* 1988; Lan and Zhang 2011b), it is necessary to impose the FSBC at the top border and the PML at other boundaries. Several studies have imposed the FSBC at the top model and the PML at others under the assumption of a flat surface (Komatitsch and Tromp 2003; Chen 2011). More recently, Liu *et al.* (2014) imposed the FSBC and the PML in their finite element method to simulate seismic wave propagation in complex geometries without expounding on how the FSBC was imposed. Numerical examples show that if the FSBC is imposed at the surface of the model, then it should also be incorporated into the PML imposed at the surface of the top-left and top-right corners of a 2D model (Fig. 1). Otherwise, significant reflections will occur at the intersections of the free surface and the PML, which is confirmed in this paper. So, in this paper, we try to construct a stable and efficient PML that can deal with irregular free surface.

We first incorporate the PML into wave equations formulated in a frequency domain in Cartesian coordinates. We then transform them back into the time domain through inverse Fourier transformation. We next map a rectangular model in curvilinear coordinates to a complex model in Cartesian coordinates. Thus, the Cartesian coordinates ( $x, z$ ) of each grid point can be determined from its curvilinear coordinates ( $q, r$ ) (Fig. 2). Afterwards, we transform the

**Figure 2** Mapping between curvilinear coordinates and Cartesian coordinates in two dimensions (after Lan and Zhang 2012).



**Figure 3** Source waveform (a) and its frequency spectrum (b).

equations and FSBC in Cartesian coordinates to curvilinear coordinates using the chain rule. By replacing the normal second derivatives in the wave equations (in the curvilinear coordinates) with the FSBC, we successfully incorporate the FSBC into the PML at the surface of the top-left and top-right corners of the 2D model. Three numerical examples are given to show the effectiveness of the PML in simulating seismic

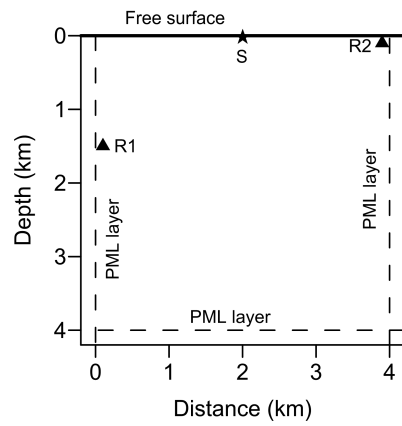


**Figure 4** Model 1 of the 2D homogeneous medium of size 4 km  $\times$  4 km. The energy source S is indicated by a black star and the receivers R1 and R2 are marked by triangles. The PML is represented by dashed lines.

wave propagation in unbounded media with an irregular free surface. We finish with some conclusions.

## METHOD

Here, we consider elastic wave propagation in a non-rectangular domain like the one depicted in the left panel of Fig. 2. In a Cartesian coordinate system, the  $x$ - $y$  system, the elastic wave equation, without external force, takes the form (Altermann and Karal 1968):

$$\rho \frac{\partial^2 u}{\partial t^2} = \frac{\partial}{\partial x} \left[ (\lambda + 2\mu) \frac{\partial u}{\partial x} + \lambda \frac{\partial v}{\partial z} \right] + \frac{\partial}{\partial z} \left[ \mu \left( \frac{\partial v}{\partial x} + \frac{\partial u}{\partial z} \right) \right], \quad (1a)$$

$$\rho \frac{\partial^2 v}{\partial t^2} = \frac{\partial}{\partial x} \left[ \mu \left( \frac{\partial v}{\partial x} + \frac{\partial u}{\partial z} \right) \right] + \frac{\partial}{\partial z} \left[ \lambda \frac{\partial u}{\partial x} + (\lambda + 2\mu) \frac{\partial v}{\partial z} \right], \quad (1b)$$

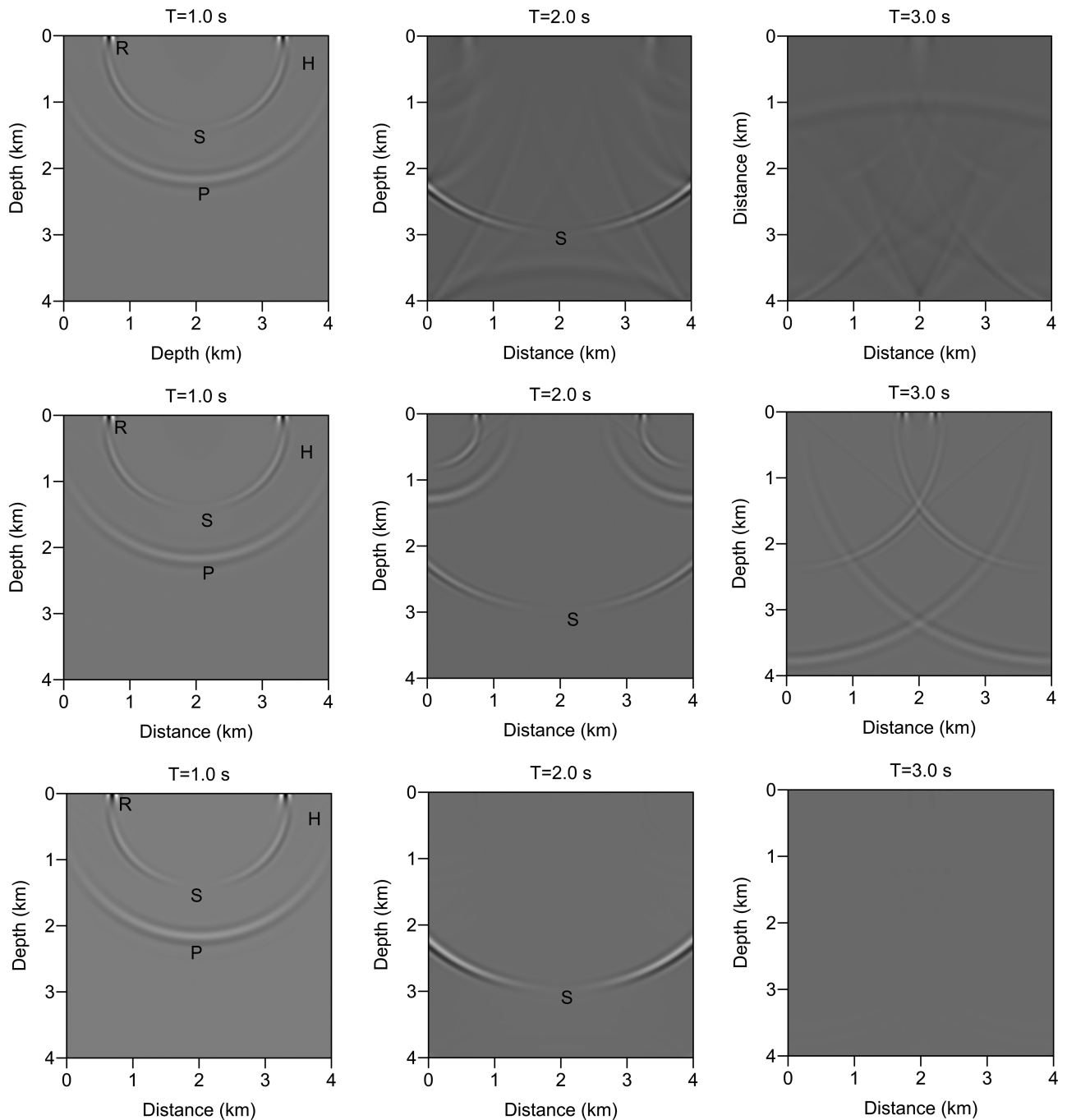


**Figure 5** Snapshots of the vertical component of the displacement obtained at 1.0 s, 2.0 s and 3.0 s for Model 1 after using the sponge boundary condition (a), PML1 (b) and PML2 (c), respectively. The compressional wave (P), shear wave (S), Rayleigh wave (R) and head wave (H) that were generated at the free surface are marked.

where  $u$  and  $v$  are the displacements in the  $x$ - and  $z$ -directions, respectively;  $\rho$  is the density;  $\lambda$  and  $\mu$  are the Lame parameters.

At the top border, the free surface boundary conditions are imposed, which can be represented as (Alterman and Rotenberg, 1969):

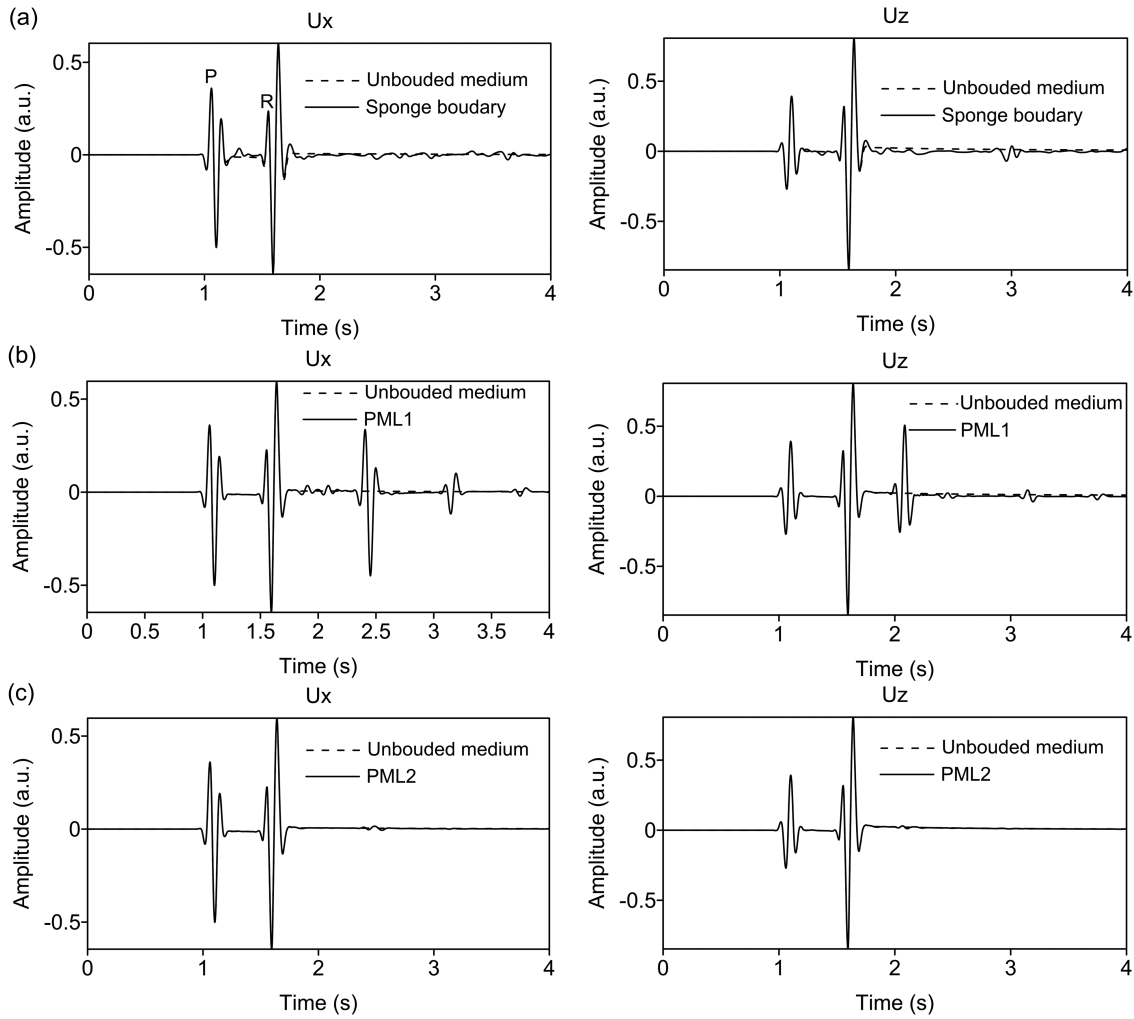


**Figure 6** Seismograms of the horizontal ( $U_x$ ) and vertical ( $U_z$ ) components of the displacement for receiver R1 in Model 1 after using the sponge boundary condition (a), PML1 (b) and PML2 (c), respectively. The dashed lines show the seismograms in an ‘unbounded medium’, which is, seismograms with no reflections included at all. The solid lines represent the results by using the sponge boundary condition (a), PML1 (b) and PML2 (c), respectively.

$$\mu \frac{\partial u}{\partial z} + \mu \frac{\partial v}{\partial x} = 0, \quad (2a)$$

$$(\lambda + 2\mu) \frac{\partial v}{\partial z} + \lambda \frac{\partial u}{\partial x} = 0. \quad (2b)$$

In order to introduce the PML into the modelling scheme, equations 1a,b can be modified using complex stretched coordinates. In the frequency domain, the complex coordinate-stretching variable is chosen as (Collino and Tsogka 2001):

$$\partial \tilde{s} = \frac{i\omega}{i\omega + d_s} \partial s, \quad (3)$$

where  $i$  is the imaginary number unit;  $\omega$  is the angular frequency;  $d_s$  is the damping coefficient along the  $s$  axis.

Substituting equation (3) into the frequency-domain form of equations (1a, b) leads to equations in complex stretched coordinates as follows:

$$\begin{aligned} \rho(i\omega)^2 U &= \frac{i\omega}{i\omega + d_x} \frac{\partial}{\partial x} \left[ (\lambda + 2\mu) \frac{i\omega}{i\omega + d_x} \frac{\partial U}{\partial x} + \lambda \frac{i\omega}{i\omega + d_z} \frac{\partial V}{\partial z} \right] \\ &\quad + \frac{i\omega}{i\omega + d_z} \frac{\partial}{\partial z} \left( \mu \frac{i\omega}{i\omega + d_x} \frac{\partial V}{\partial x} + \mu \frac{i\omega}{i\omega + d_z} \frac{\partial U}{\partial z} \right), \end{aligned} \quad (4a)$$

$$\begin{aligned} \rho(i\omega)^2 V &= \frac{i\omega}{i\omega + d_x} \frac{\partial}{\partial x} \left( \mu \frac{i\omega}{i\omega + d_x} \frac{\partial V}{\partial x} + \mu \frac{i\omega}{i\omega + d_z} \frac{\partial U}{\partial z} \right) \\ &\quad + \frac{i\omega}{i\omega + d_z} \frac{\partial}{\partial z} \left[ \lambda \frac{i\omega}{i\omega + d_x} \frac{\partial U}{\partial x} + (\lambda + 2\mu) \frac{i\omega}{i\omega + d_z} \frac{\partial V}{\partial z} \right], \end{aligned} \quad (4b)$$

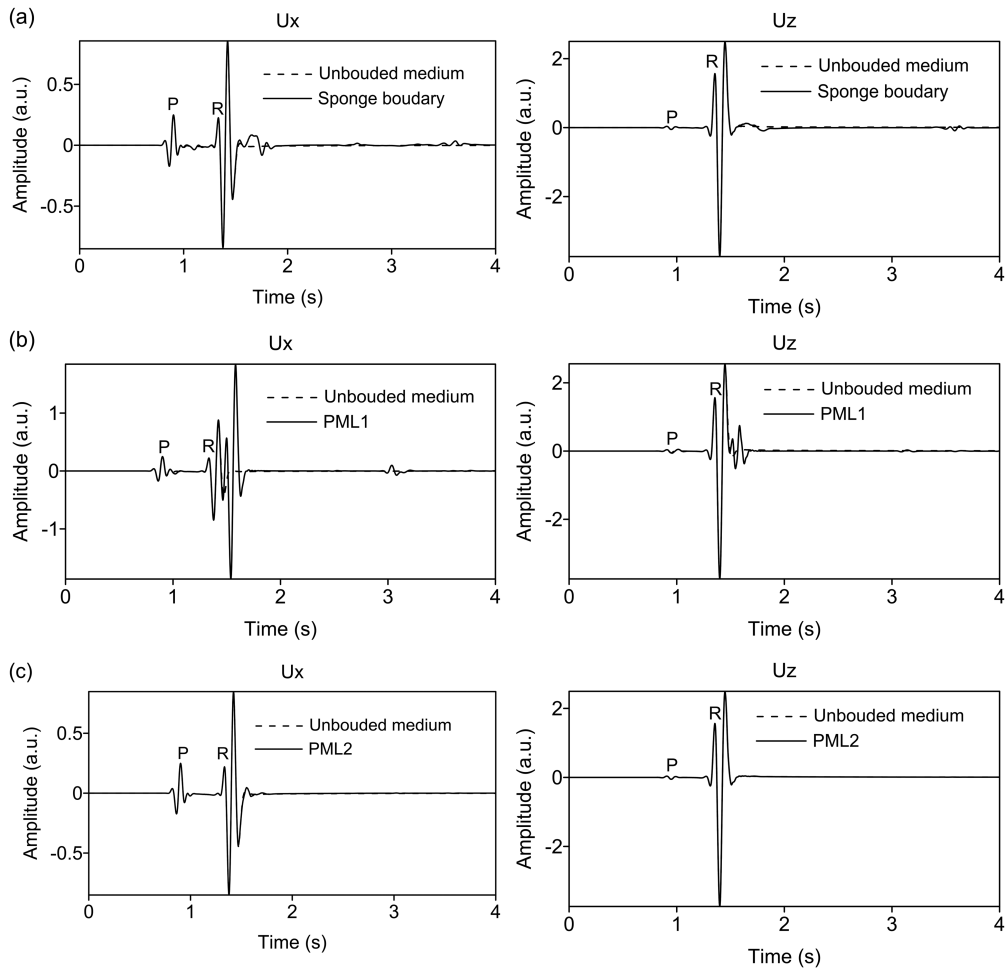


**Figure 7** Seismograms of the horizontal ( $U_x$ ) and vertical ( $U_z$ ) components of the displacement for receiver R2 in Model 1 after using the sponge boundary condition (a), the PML1 (b) and the PML2 (c), respectively. The dashed lines show the seismograms in an ‘unbounded medium’. The solid lines represent the results by using the sponge boundary condition (a), PML1 (b) and PML2 (c), respectively.

where  $U$  and  $V$  are the Fourier transforms of  $u$  and  $v$  with respect to the time variable  $t$ , respectively;  $d_x = -(n+1) \cdot \log(R) \cdot \frac{V_p}{2l} \cdot (\frac{x}{l})^2$  (Collino and Tsogka 2001) is the damping coefficient along the  $x$  axis, where  $V_p$  is the pressure-wave velocity,  $l$  is the thickness of the PML,  $x$  is the horizontal distance from the mesh grid to the inner boundaries of the PML,  $n$  is a constant that controls the changing rate of the damping coefficients,  $R$  is the theoretical reflection coefficient;  $d_z$  has a similar expression as that of  $d_x$ , where  $x$  is replaced by  $z$ . According to Komatsch and Martin (2007), we take  $n = 2$ ,  $R = 0.001$  for implementation of the PML.

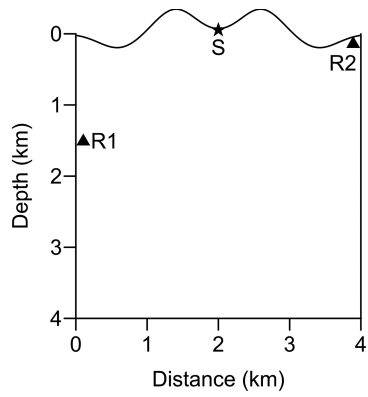


**Figure 8** Frame diagram of Model 2. The energy source S is indicated by a black-filled pentagram and the receivers R1 and R2 are marked by triangles. The PMLs with a width of 20 grids are not included in the frame.

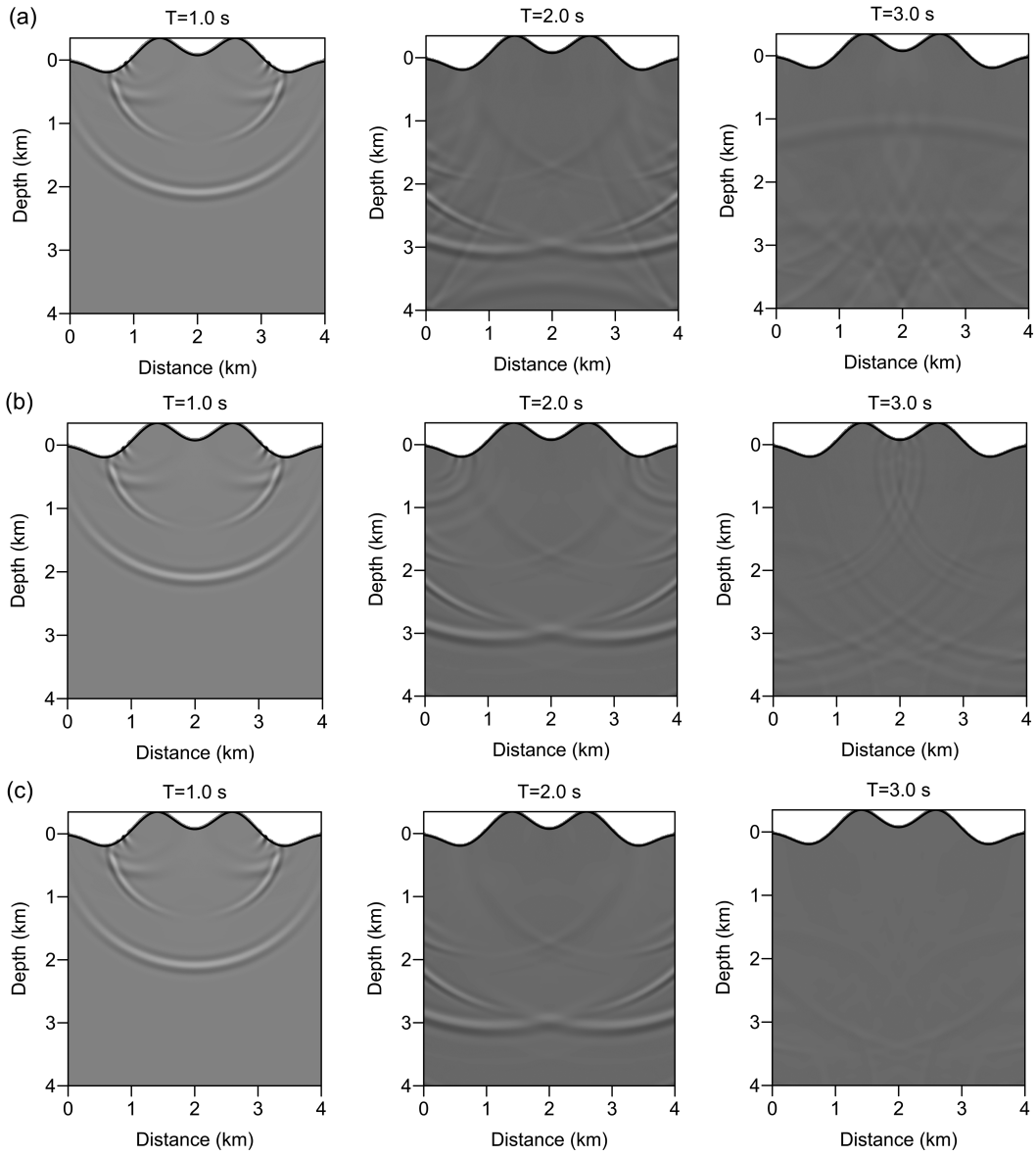


**Figure 9** Snapshots of the vertical component of the displacement obtained at 1.0 s, 2.0 s and 3.0 s for Model 2 after using the sponge boundary condition (a), PML1 (b) and PML2 (c), respectively.

We split expressions (4a, b) into three terms, respectively and rewrite them as:

$$\left\{ \begin{array}{l} \rho(i\omega + d_x)^2 U_1 = \frac{\partial}{\partial x} [(\lambda + 2\mu) \frac{\partial U}{\partial x}] + P_{xx} \\ \rho(i\omega + d_x)(i\omega + d_z)U_2 = [\frac{\partial}{\partial x} (\lambda \frac{\partial V}{\partial z}) + \frac{\partial}{\partial z} (\mu \frac{\partial V}{\partial x})] \\ \rho(i\omega + d_z)^2 U_3 = \frac{\partial}{\partial z} (\mu \frac{\partial U}{\partial z}) + P_{zz} \\ (i\omega + d_x)P_{xx} = -(\lambda + 2\mu)d'_x \frac{\partial U}{\partial x} \\ (i\omega + d_z)P_{xz} = -\mu d'_z \frac{\partial U}{\partial z} \end{array} \right., \quad (5a)$$

$$\left\{ \begin{array}{l} \rho(i\omega + d_x)^2 V_1 = \frac{\partial}{\partial x} (\mu \frac{\partial V}{\partial x}) + P_{zx} \\ \rho(i\omega + d_x)(i\omega + d_z) V_2 = [\frac{\partial}{\partial x} (\mu \frac{\partial U}{\partial z}) + \frac{\partial}{\partial z} (\lambda \frac{\partial U}{\partial x})] \\ \rho(i\omega + d_z)^2 V_3 = \frac{\partial}{\partial z} [(\lambda + 2\mu) \frac{\partial V}{\partial z}] + P_{zz} \\ (i\omega + d_x)P_{zx} = -\mu d'_x \frac{\partial V}{\partial x} \\ (i\omega + d_z)P_{zz} = -(\lambda + 2\mu)d'_z \frac{\partial V}{\partial z} \end{array} \right., \quad (5b)$$

where  $U = U_1 + U_2 + U_3$  and  $V = V_1 + V_2 + V_3$ ,  $P_{xx}$ ,  $P_{xz}$ ,  $P_{zx}$ ,  $P_{zz}$  are introduced intermediate variables;  $d'_x = \frac{\partial d_x}{\partial x}$  and

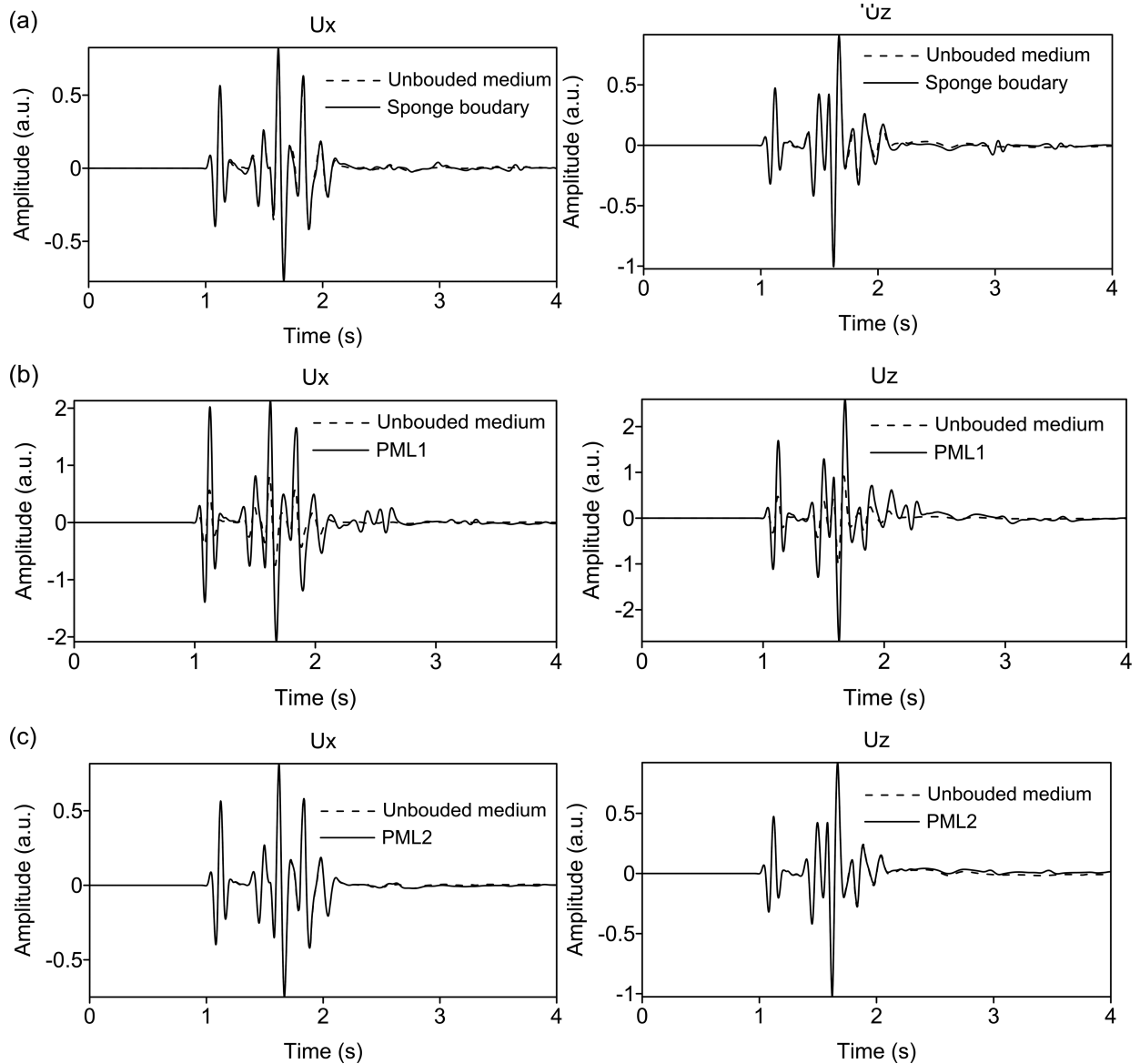


Figure 10 Seismograms of the horizontal ( $U_x$ ) and vertical ( $U_z$ ) components of the displacement for receiver R1 in Model 2 after using the sponge boundary condition (a), PML1 (b) and PML2 (c), respectively. The dashed lines show the seismograms in an ‘unbounded medium’. The solid lines represent the results by using the sponge boundary condition (a), PML1 (b) and PML2 (c), respectively.

$d'_z = \frac{\partial d_z}{\partial z}$ , with  $d_x$  and  $d_z$  defined in equations (4a, b). Transforming them back into the time domain, we can obtain the following expressions:

$$\left\{ \begin{array}{l} \rho(\partial_t + d_x)^2 u_1 = \frac{\partial}{\partial x} \left[ (\lambda + 2\mu) \frac{\partial u}{\partial x} \right] + p_{xx} \\ \rho(\partial_t + d_x)(\partial_t + d_z)u_2 = \left[ \frac{\partial}{\partial x} \left( \lambda \frac{\partial v}{\partial z} \right) + \frac{\partial}{\partial z} \left( \mu \frac{\partial v}{\partial x} \right) \right] \\ \rho(\partial_t + d_z)^2 u_3 = \frac{\partial}{\partial z} \left( \mu \frac{\partial u}{\partial z} \right) + p_{zz} \\ (\partial_t + d_x)p_{xx} = -(\lambda + 2\mu)d_x' \frac{\partial u}{\partial x} \\ (\partial_t + d_z)p_{xz} = -\mu d_z' \frac{\partial u}{\partial z} \end{array} \right., \quad (6a)$$

$$\left\{ \begin{array}{l} \rho(\partial_t + d_x)^2 v_1 = \frac{\partial}{\partial x} \left( \mu \frac{\partial v}{\partial x} \right) + p_{zx} \\ \rho(\partial_t + d_x)(\partial_t + d_z)v_2 = \left[ \frac{\partial}{\partial x} \left( \mu \frac{\partial u}{\partial z} \right) + \frac{\partial}{\partial z} \left( \lambda \frac{\partial u}{\partial x} \right) \right] \\ \rho(\partial_t + d_z)^2 v_3 = \frac{\partial}{\partial z} \left[ (\lambda + 2\mu) \frac{\partial v}{\partial z} \right] + p_{zz} \\ (\partial_t + d_x)p_{zx} = -\mu d_x' \frac{\partial v}{\partial x} \\ (\partial_t + d_z)p_{zz} = -(\lambda + 2\mu)d_z' \frac{\partial v}{\partial z} \end{array} \right., \quad (6b)$$

where  $u = u_1 + u_2 + u_3$  and  $v = v_1 + v_2 + v_3$ ,  $p_{xx}$ ,  $p_{xz}$ ,  $p_{zx}$ ,  $p_{zz}$  are inverse forms of  $P_{xx}$ ,  $P_{xz}$ ,  $P_{zx}$ ,  $P_{zz}$  in the time domain. The computational domain is divided into two parts, namely,

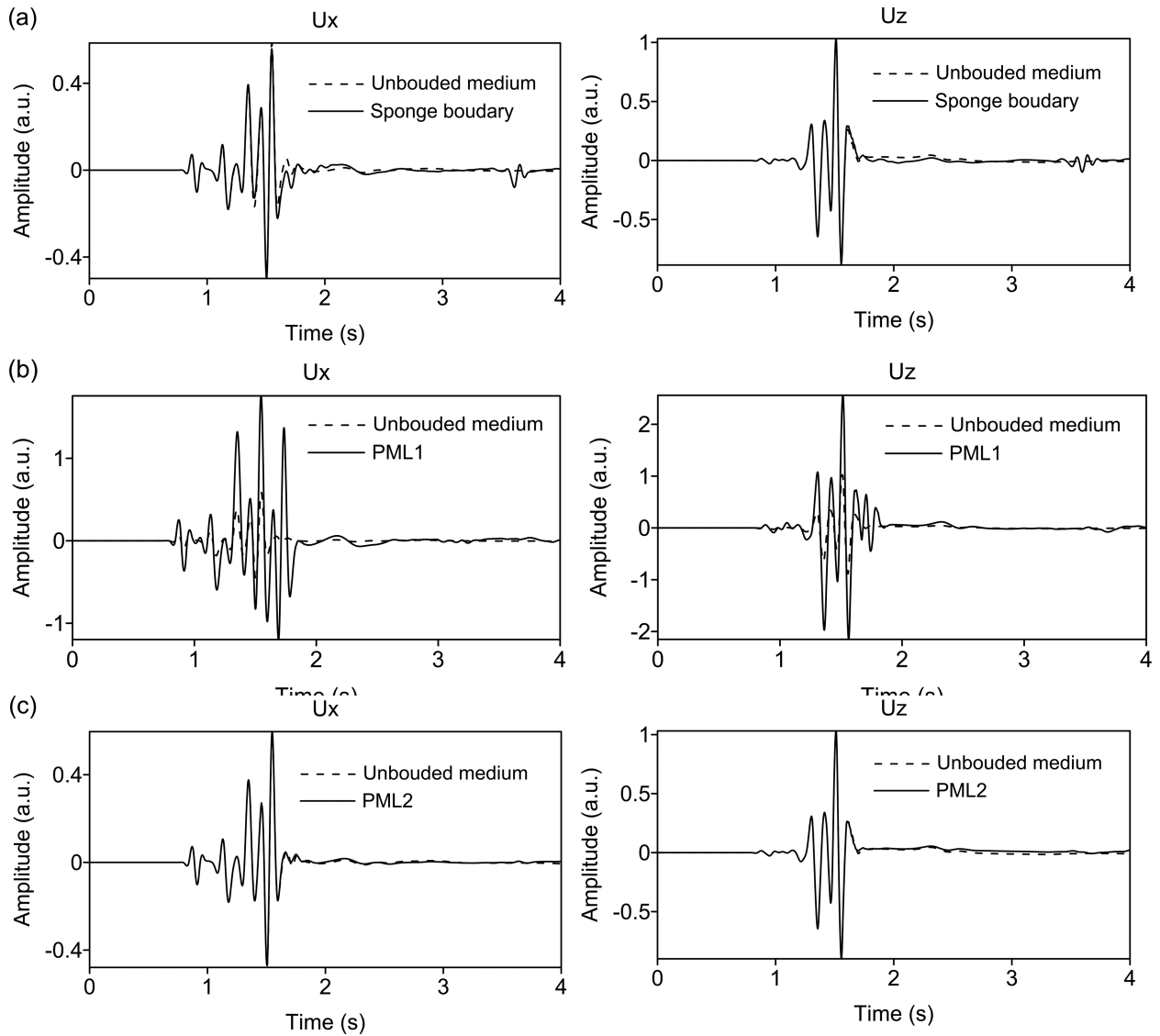


Figure 11 Seismograms of the horizontal ( $U_x$ ) and vertical ( $U_z$ ) components of the displacement for receiver R2 in Model 2 after using the sponge boundary condition (a), PML1 (b) and PML2 (c), respectively. The dashed lines show the seismograms in an ‘unbounded medium’. The solid lines represent the results by using the sponge boundary condition (a), PML1 (b) and PML2 (c), respectively.

the regular or main domain and the PML absorbing domain. In the regular domain,  $d_x = d_z = 0$ , where expressions (6a, b) are degenerated to standard elastic wave equations (1a, b); whereas in the PML,  $d_x \neq 0$ ,  $d_z \neq 0$ , which can attenuate the spurious reflections effectively.

For a given topographic surface, the discrete grid should conform to the free surface in order to suppress artificial scattered waves. Such a grid is termed as the ‘boundary conforming grid’ (Hvid 1994) and has been used by a number of researchers in the simulation of seismic wavefields (Appelo and Petersson 2009; Lan and Zhang 2011a; Rao and Wang

2013). A grid of this type can be generated by carrying out a transformation from curvilinear coordinates to Cartesian coordinates.

After generating the boundary conforming grids, the Cartesian coordinates of every grid point can be determined from its curvilinear coordinates. We then can express the spatial derivatives in the Cartesian coordinate system ( $x$ ,  $z$ ) from the curvilinear coordinate system ( $q$ ,  $r$ ) following the chain rule:

$$\partial_x = q_x \partial_q + r_x \partial_r, \quad \partial_z = q_z \partial_q + r_z \partial_r, \quad (7)$$

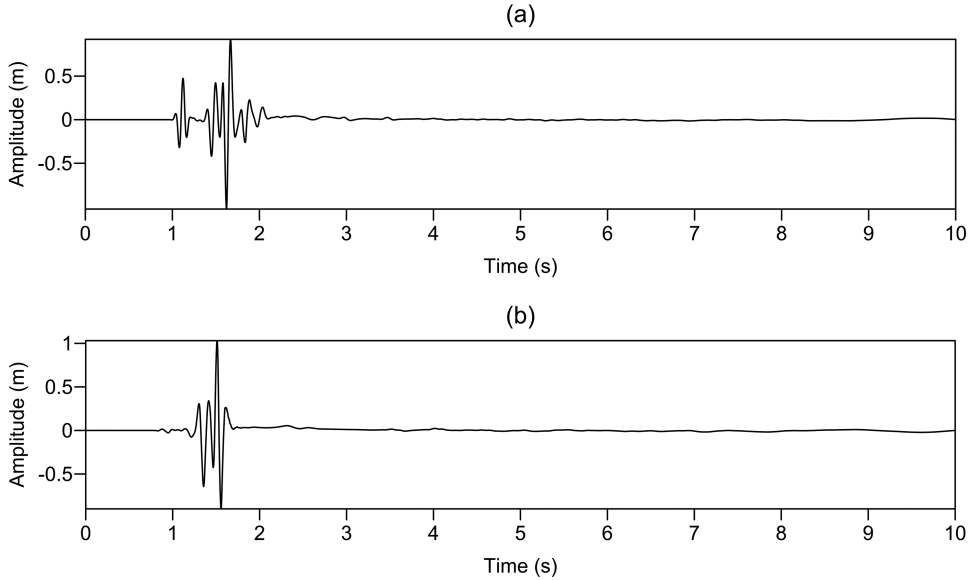


Figure 12 Seismograms of the vertical component of the displacement for receivers R1 (a) and R2 (b) in Model 2 after using PML2 in long-time simulation.

where  $q_x$  denotes  $\partial q(x, z)/\partial x$  and other items express similar meanings. Utilizing relationships (7), the wave equations (6a, b) can be transformed into the following forms:

$$\left\{ \begin{array}{l} \rho(\partial_t + d_x)^2 u_1 \\ = (\lambda + 2\mu)(q_x^2 \partial_q^2 u + 2q_x r_x \partial_q \partial_r u + r_x^2 \partial_r^2 u) + p_{xx} \\ \rho(\partial_t + d_x)(\partial_t + d_z) u_2 \\ = (\lambda + \mu)[q_x q_z \partial_q^2 v + (q_x r_z + r_x q_z) \partial_q \partial_r v + r_x r_z \partial_r^2 v], \end{array} \right. \quad (8a)$$

$$\left\{ \begin{array}{l} \rho(\partial_t + d_z)^2 u_3 = \mu(q_z^2 \partial_q^2 u + 2q_z r_z \partial_q \partial_r u + r_z^2 \partial_r^2 u) + p_{xz} \\ (\partial_t + d_x)p_{xx} = -(\lambda + 2\mu)d_x'(q_x \partial_q u + r_x \partial_r u) \\ (\partial_t + d_z)p_{xz} = -\mu d_z'(q_z \partial_q u + r_z \partial_r u) \end{array} \right. \quad (8b)$$

and

$$\left\{ \begin{array}{l} \rho(\partial_t + d_x)^2 v_1 = \mu(q_x^2 \partial_q^2 v + 2q_x r_x \partial_q \partial_r v + r_x^2 \partial_r^2 v) + p_{zx} \\ \rho(\partial_t + d_x)(\partial_t + d_z) v_2 \\ = (\lambda + \mu)[q_x q_z \partial_q^2 u + (q_x r_z + r_x q_z) \partial_q \partial_r u + r_x r_z \partial_r^2 u] \\ \rho(\partial_t + d_z)^2 v_3 \\ = (\lambda + 2\mu)(q_z^2 \partial_q^2 v + 2q_z r_z \partial_q \partial_r v + r_z^2 \partial_r^2 v) + p_{zz} \\ (\partial_t + d_x)p_{zx} = -\mu d_x'(q_x \partial_q v + r_x \partial_r v) \\ (\partial_t + d_z)p_{zz} = -(\lambda + 2\mu)d_z'(q_z \partial_q v + r_z \partial_r v) \end{array} \right. \quad (8b)$$

Similarly, the free surface boundary conditions (2a, b) can be transformed to (Lan and Zhang 2011a):

$$\begin{aligned} &[(\lambda + 2\mu)r_x^2 + \mu r_z^2]\partial_r u + [(\lambda + 2\mu)q_x r_x + \mu q_z r_z]\partial_q u, \\ &+(\lambda + \mu)r_x r_z \partial_r v + [\mu q_x r_z + \lambda q_z r_x]\partial_q v = 0 \end{aligned} \quad (9a)$$

$$\begin{aligned} &[\mu r_x^2 + (\lambda + 2\mu)r_z^2]\partial_r v + [\mu q_x r_x + (\lambda + 2\mu)q_z r_z]\partial_q v \\ &+(\lambda + \mu)r_x r_z \partial_r u + [\lambda q_x r_z + \mu q_z r_x]\partial_q u = 0 \end{aligned} \quad (9b)$$

We could add the first three equations of sets (8a) and (8b) together respectively and then approximate the normal second derivatives with a central difference. If we take the equations of system (8a) as an example, we obtain:

$$\begin{aligned} &\rho(\partial_t + d_x)^2 u_1 + \rho(\partial_t + d_x)(\partial_t + d_z)u_2 + \rho(\partial_t + d_z)^2 u_3 \\ &= (\lambda + 2\mu)\left(q_x^2 \partial_q^2 u + 2q_x r_x \partial_q \partial_r u + r_x^2 \frac{\partial u_{i,j+1} - 2u_{i,j}}{\partial r^2}\right) + p_{xx} \\ &+ (\lambda + \mu)\left[q_x q_z \partial_q^2 v + (q_x r_z + r_x q_z) \partial_q \partial_r v + r_x r_z \frac{\partial v_{i,j+1} - 2v_{i,j}}{\partial r^2}\right], \\ &+ \mu\left(q_z^2 \partial_q^2 u + 2q_z r_z \partial_q \partial_r u + r_z^2 \frac{\partial u_{i,j+1} - 2u_{i,j}}{\partial r^2}\right) + p_{xz} \\ &+ [(\lambda + 2\mu)r_x^2 + \mu r_z^2]\frac{\partial u_{i,j-1}}{\partial r^2} + (\lambda + \mu)r_x r_z \frac{\partial v_{i,j-1}}{\partial r^2} \end{aligned} \quad (10)$$

where  $i$  and  $j$  are the grid points in the  $q$ - and  $r$ -directions, respectively;  $\partial r$  is the grid size in the  $r$  direction.

We also use the central difference to approximate the normal derivatives in the free surface boundary conditions (9a, b). Take equation (9a) for example, which can be arranged as follows:

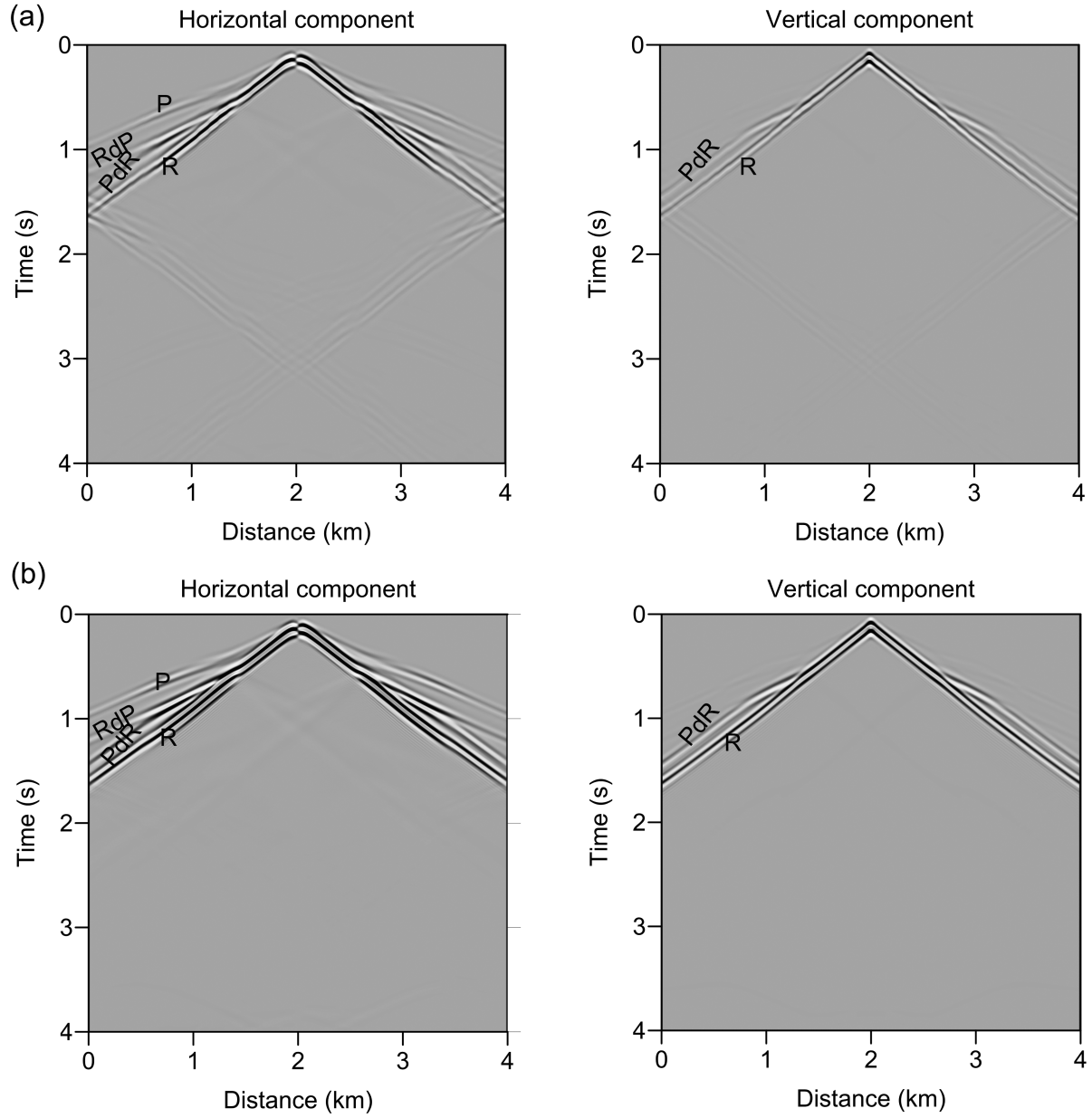


Figure 13 Synthetic seismic profiles of the horizontal and vertical components of the displacement for Model 2 after using PML1 (a) and PML2 (b), respectively. P denotes the direct compressional wave, R denotes the direct Rayleigh wave, PdR denotes the P-wave diffracted to the Rayleigh wave, while RdP represents the Rayleigh wave diffracted to the P-wave.

$$\begin{aligned}
 & [(\lambda + 2\mu)r_x^2 + \mu r_z^2] \frac{u_{i,j-1}}{dr^2} + (\lambda + \mu)r_x r_z \frac{v_{i,j-1}}{dr^2} \\
 & = [(\lambda + 2\mu)r_x^2 + \mu r_z^2] \frac{u_{i,j+1}}{dr^2} \\
 & + 2[(\lambda + 2\mu)q_x r_x + \mu q_z r_z] \frac{\partial_q u}{dr} \\
 & + (\lambda + \mu)r_x r_z \frac{v_{i,j+1}}{dr^2} + 2(\mu q_x r_z + \lambda q_z r_x) \frac{\partial_q v}{dr}
 \end{aligned} \quad (11)$$

Observing the above two equations we find that the last line of equation (10) and the left part of equation (11) are exactly the same. We use the right part of equation (11) to replace the last line of equation (10) and then break it into three items again leading to:

$$\left\{ \begin{array}{l} \rho(\partial_t + d_x)^2 u_1 \\ = (\lambda + 2\mu) \left( q_x^2 \partial_q^2 u + 2q_x r_x \partial_q \partial_r u + 2r_x^2 \frac{u_{i,j+1} - u_{i,j}}{dr^2} \right) + p_{xx} \\ \rho(\partial_t + d_x)(\partial_t + d_z) u_2 \\ = (\lambda + \mu) \left[ q_x q_z \partial_q^2 v + (q_x r_z + r_x q_z) \partial_q \partial_r v + 2r_x r_z \frac{v_{i,j+1} - v_{i,j}}{dr^2} \right] \\ + 2[(\lambda + 2\mu) q_x r_x + \mu q_z r_z] \frac{\partial_q u}{dr} + 2(\mu q_x r_z + \lambda q_z r_x) \frac{\partial_q v}{dr} . \\ \rho(\partial_t + d_z)^2 u_3 \\ = \mu \left( q_z^2 \partial_q^2 u + 2q_z r_z \partial_q \partial_r u + 2r_z^2 \frac{u_{i,j+1} - u_{i,j}}{dr^2} \right) + p_{xz} \\ (\partial_t + d_x) p_{xx} = -(\lambda + 2\mu) d_x' (q_x \partial_q u + r_x \partial_r u) \\ (\partial_t + d_z) p_{xz} = -\mu d_z' (q_z \partial_q u + r_z \partial_r u) \end{array} \right. \quad (12a)$$

These set of equations are the implementations for the PML boundary condition for the horizontal component of displacement in the curvilinear coordinates, with the free surface boundary condition satisfied as well. Similarly, for the vertical component, we obtain the following equations for the PML boundary condition:

$$\left\{ \begin{array}{l} \rho(\partial_t + d_x)^2 v_1 \\ = \mu \left( q_x^2 \partial_q^2 v + 2q_x r_x \partial_q \partial_r v + 2r_x^2 \frac{v_{i,j+1} - v_{i,j}}{dr^2} \right) + p_{zx} \\ \rho(\partial_t + d_x)(\partial_t + d_z) v_2 \\ = (\lambda + \mu) \left[ q_x q_z \partial_q^2 u + (q_x r_z + r_x q_z) \partial_q \partial_r u + 2r_x r_z \frac{u_{i,j+1} - u_{i,j}}{dr^2} \right] \\ + 2[\mu q_x r_x + (\lambda + 2\mu) q_z r_z] \frac{\partial_q v}{dr} + 2(\lambda q_x r_z + u q_z r_x) \frac{\partial_q u}{dr} . \\ \rho(\partial_t + d_z)^2 v_3 \\ = (\lambda + 2\mu) \left( q_z^2 \partial_q^2 v + 2q_z r_z \partial_q \partial_r v + 2r_z^2 \frac{v_{i,j+1} - v_{i,j}}{dr^2} \right) + p_{zz} \\ (\partial_t + d_x) p_{zx} = -\mu d_x' (q_x \partial_q v + r_x \partial_r v) \\ (\partial_t + d_z) p_{zz} = -(\lambda + 2\mu) d_z' (q_z \partial_q v + r_z \partial_r v) \end{array} \right. \quad (12b)$$

We use the forward difference of first order to approximate the normal derivative ( $\partial_r$ ) in the cross derivatives ( $\partial_q \partial_r$  and  $\partial_r \partial_q$ ). The central difference is used to approximate the horizontal derivatives ( $\partial_q$ ) in the calculation of equations (12a, b). In addition, the central difference is used for the spatial discretization in regions other than the boundaries (Lan and Zhang 2011a).

In the following, we will investigate the validity and efficiency of the PML constructed in this paper in attenuating boundary reflections in seismic wavefield modelling with an irregular free surface and compare it with the sponge boundary condition as used in previous studies. The sponge boundary condition  $G$  is defined as (Lan and Zhang 2012):

$$G = \exp[-\alpha(I - i)^2], \quad 1 \leq i \leq I, \quad (13)$$

where  $I$  is the width in nodes of the sponge boundary;  $i$  is the node number and  $\alpha$  is the modulus decay factor.

## EXAMPLES

We perform numerical experiments on three models to illustrate the effectiveness of the PML in the simulation of seismic wave propagation in unbounded media with an irregular surface. We first design a model with a flat surface that we denote as Model 1. Second, a model with complex surface topography is used that is designated as Model 2. We then move the source in Model 2 to the centre of the domain to test the method for different incident angles, which we name as Model 3. These models are set to be homogeneous in order to discern the boundary reflections more clearly if the boundary conditions do not work well. The P-wave velocity is 2500 m/s, the S-wave velocity is 1600 m/s and the density is 1800 kg/m<sup>3</sup>. A vertical point source of Gabor wavelet described by the following expression is used in the numerical experiments (Kristek, Moczo and Archuleta 2002):

$$f(t) = e^{-0.5 f_0^2 (t-t_0)^2} \cos \pi f_0 (t-t_0), \quad (14)$$

with time delay  $t_0 = 0.12$  s and a high cut-off frequency  $f_0 = 25$  Hz (Fig. 3).

### Model 1

The size of the flat surface model is 4.0 km × 4.0 km. The grid spacings are 10 m in both the horizontal and vertical directions. The time interval is 1 ms and the total propagation time is 4 s. The seismic source is located at coordinates (2000 m, 20 m). Two receivers R1 and R2 recording the x and z components of the displacement are placed at coordinates (100 m, 1500 m) and (3900 m, 100 m), respectively. The receivers are close to the model boundaries (Fig. 4), thus, it is easier to recognize the strongly spurious reflections from the model boundaries if the boundary conditions do not work well. In Fig. 4, the black star indicates the source S and the two triangles indicate the two receivers R1 and R2, respectively. During the modelling, the width for both the PMLs and the sponge boundary is 200 m (20 grids). The decay factor used in the sponge boundary takes the value of 0.015 (Lan and Zhang 2011a).

Figure 5 shows snapshots of the vertical component of the wavefields at 1.0 s, 2.0 s and 3.0 s by using the sponge boundary condition (Fig. 5a) and the PML constructed with no free surface boundary condition (FSBC) embedded at the surface of the top-left and top-right corners, which we mark

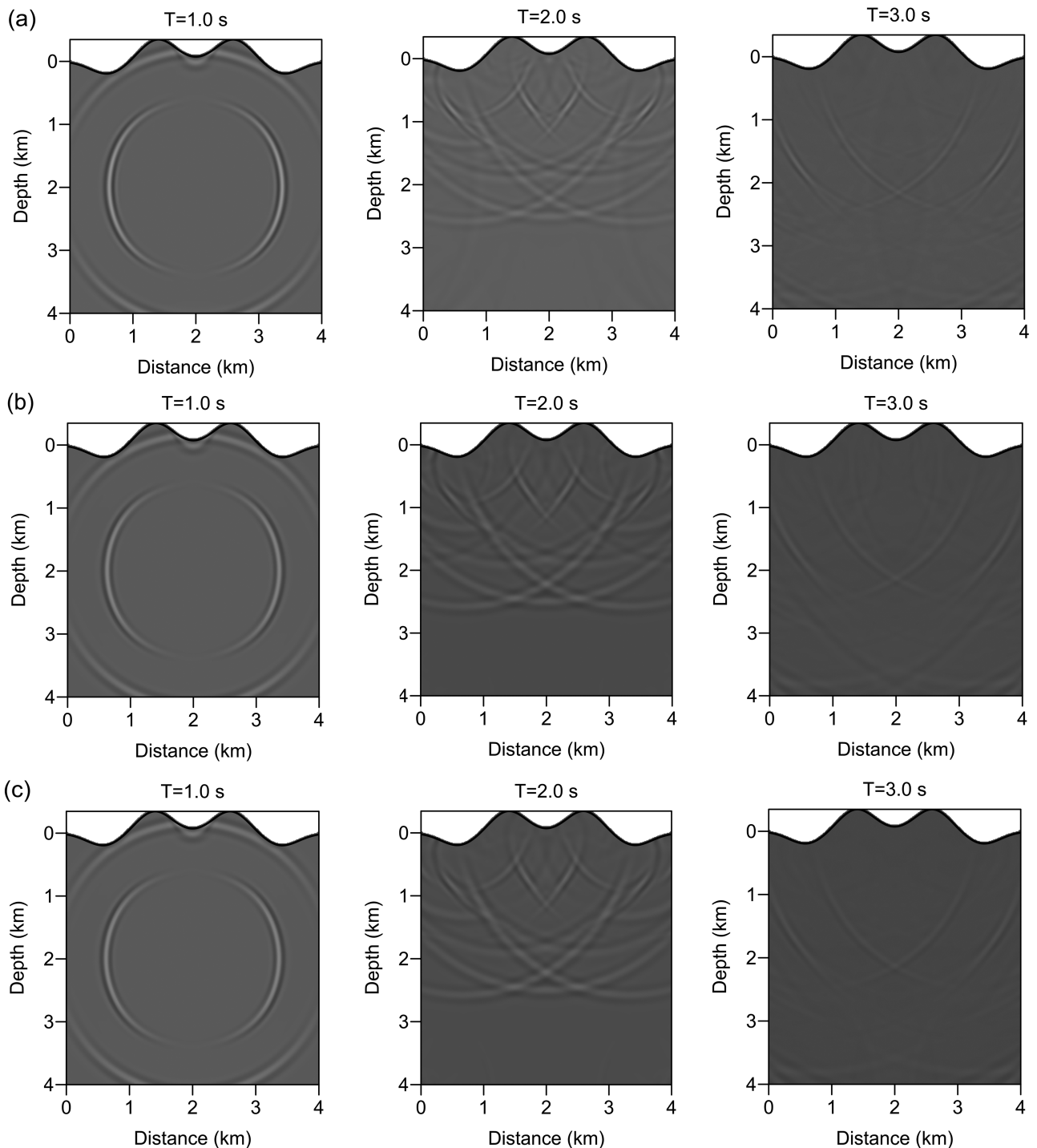


Figure 14 Snapshots of the vertical component of the displacement obtained at 1.0 s, 3.0 s and 4.0 s for Model 3 after using the sponge boundary condition (a), PML1 (b) and PML2 (c), respectively.

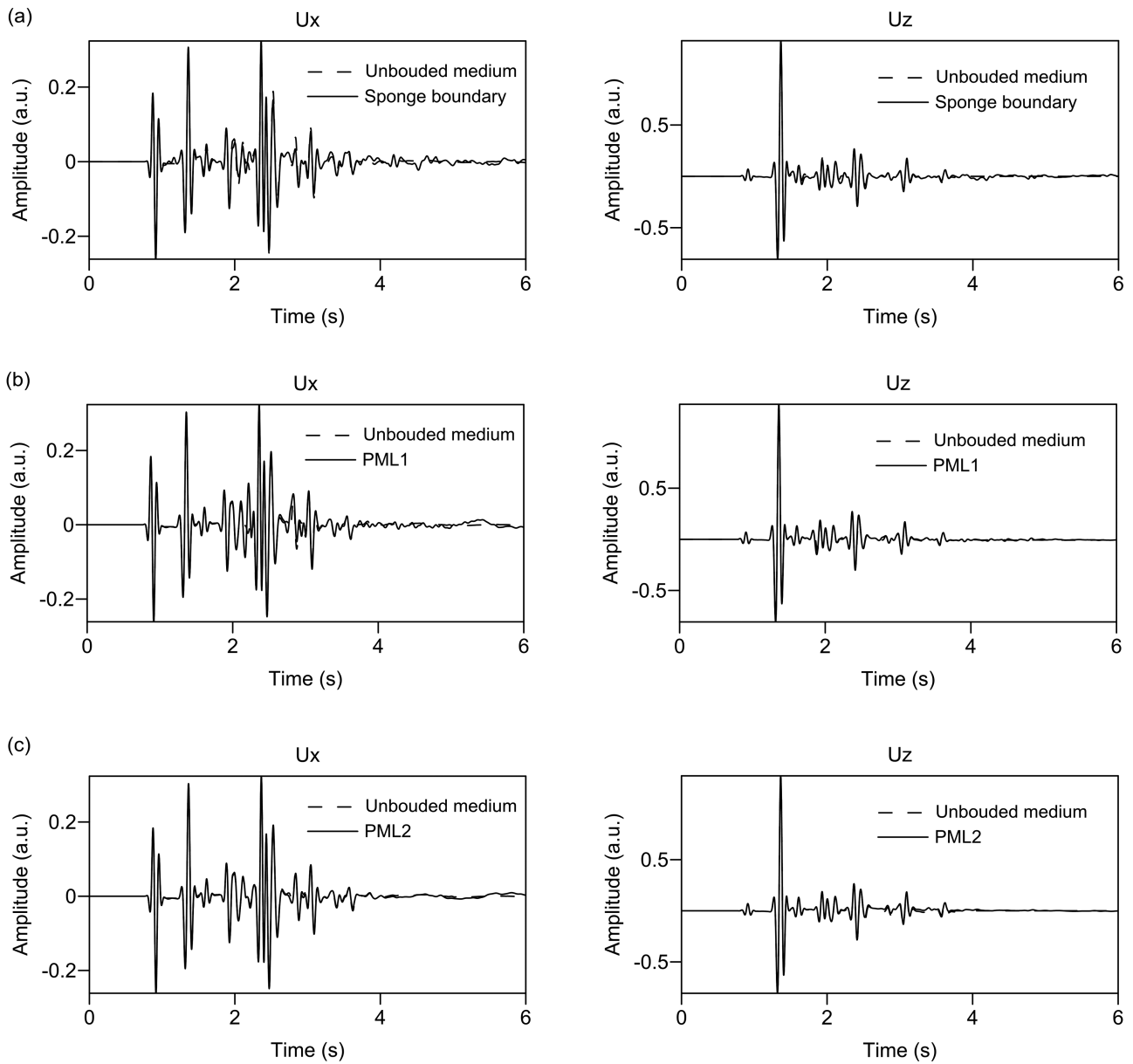
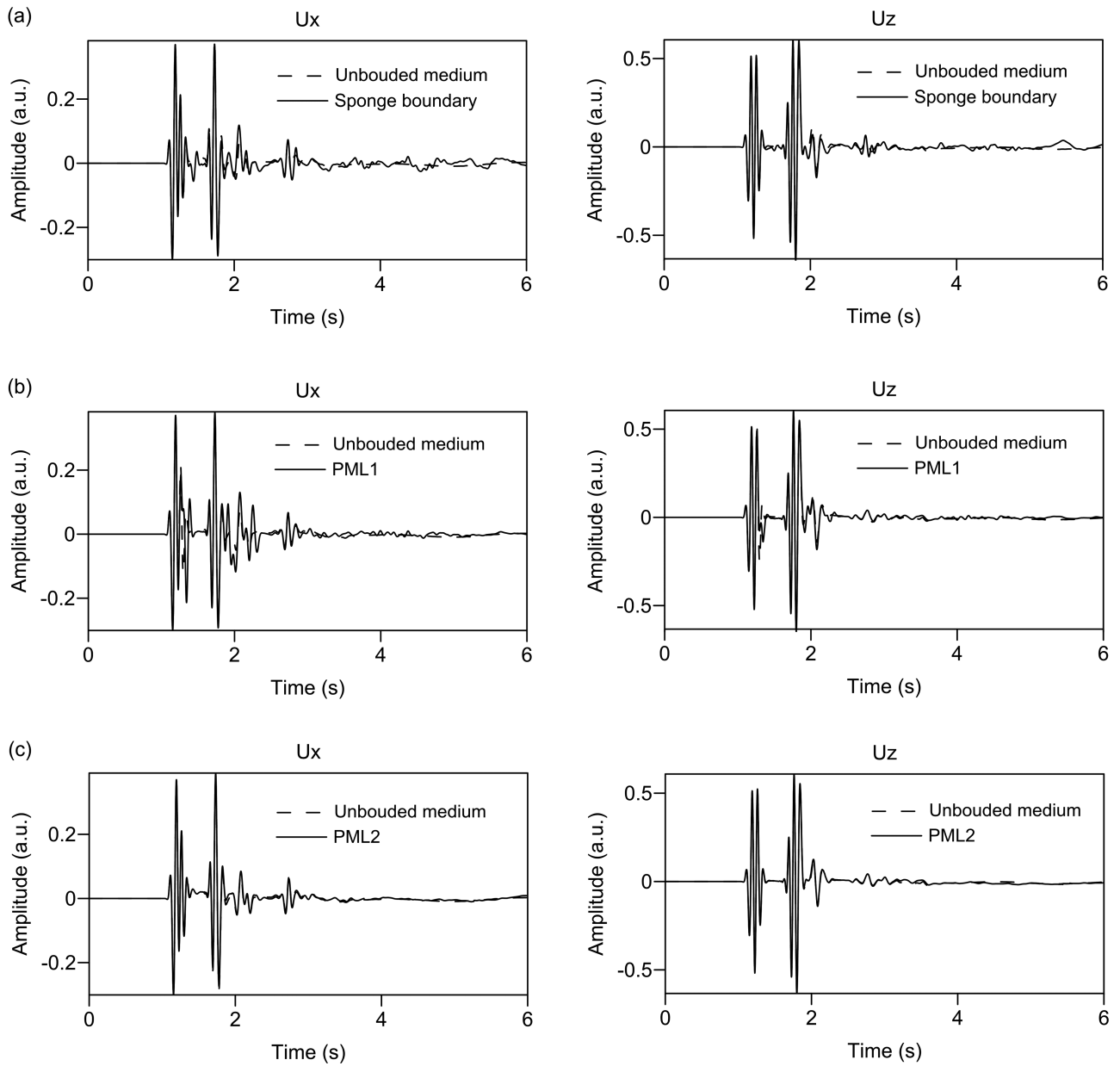


Figure 15 Seismograms of the horizontal ( $U_x$ ) and vertical ( $U_z$ ) components of the displacement for receiver R1 in Model 3 after using the sponge boundary condition (a), PML1 (b) and PML2 (c), respectively. The dashed lines show the seismograms in an ‘unbounded medium’. The solid lines represent the results by using the sponge boundary condition (a), PML1 (b) and PML2 (c), respectively.

as PML1 (Fig. 5b). Another one with the FSBC ingeniously included at the surface of the two corners, we mark as PML2 (Fig. 5c). Rayleigh waves with strong energies propagating along the surface are observed in the snapshots. As the velocity of the Rayleigh wave is very close to that of the shear wave, the two are almost superimposed and it is difficult to distinguish them in the snapshots and seismograms. We can see that apparent reflections are generated from

boundaries where the sponge boundary condition is used. Strong reflections, which are mainly surface waves, are also observed at the intersections of the free surface in the main domain and the PML inner boundaries for PML1. The reason is that the FSBC is not imposed into PMLs at the top-left and top-right corners of the model, which means the surface waves cannot propagate and be attenuated in the PMLs. For PML2, no apparent reflections are found, which indicates



**Figure 16** Seismograms of the horizontal ( $U_x$ ) and vertical ( $U_z$ ) components of the displacement for receiver R2 in Model 3 after using the sponge boundary condition (a), PML1 (b) and PML2 (c), respectively. The dashed lines show the seismograms in an ‘unbounded medium’. The solid lines represent the results by using the sponge boundary condition (a), PML1 (b) and PML2 (c), respectively.

that the latter absorbs all outgoing P, S and Rayleigh waves effectively.

We check the qualities of the PMLs by comparing the specific seismograms of receivers R1 and R2 with those calculated on a large model with no reflections recorded. Figures 6 and 7 illustrate the seismograms of the x and z

components of the wavefields recorded at receivers R1 and R2, respectively. We find spurious reflections occurred in the seismograms by using the sponge boundary condition (Figs 6a and 7a) and significant reflections from PML1 are also found in the seismograms (Figs 6b and 7b), while PML2 gives rather good results without apparent reflections (Figs 6c and 7c).

## Model 2

We change the flat surface in Model 1 to an irregular surface that combines two hills with two depressions. The surface undulation is between  $-0.35$  km and  $0.2$  km. We discretize the model with a grid size  $401 \times 401$ . The same source as used in the flat surface model is located at (2000 m, 54 m). Two receivers R1 and R2 are also employed in this model and marked by triangles in Fig. 8.

Figure 9 represents snapshots of the vertical component of the wavefields, which highlight the complications of realistic seismic wave propagation in the vicinity of the earth surface. These snapshots also show that PML2 performs very well in absorbing seismic waves (Fig. 9c), while PML1 (Fig. 9b) and the sponge boundary condition (Fig. 9a) behave poorly, especially for absorbing surface waves.

Figures 10 and 11 illustrate the seismograms of the horizontal and vertical components of the wavefields recorded at receivers R1 and R2, respectively. We find undesirable reflections occurred in the seismograms by using PML1 (Figs 10b and 11b), while the results with PML2 match very well with the theoretic results (Figs 10c and 11c) and much better than the sponge boundary condition (Figs 10a and 11a) in attenuating outgoing waves. Figure 12 shows the seismograms of the vertical component of displacement for receivers R1 and R2 by using PML2 in long-time simulation, which highlights the stability and efficiency of PML2 in outgoing waves absorption.

Figure 13 illustrates the synthetic seismic profiles of the horizontal and vertical components of the displacement with PML1 and PML2, respectively, which provide further support to the conclusions drawn above.

## Model 3

We move the source in Model 2 to the centre of the model to test the PMLs further. This test covers different incident angles. Figure 14 shows snapshots of the vertical component of the wavefields. At 1.0 s, the direct P-wave arrives at the boundaries of the model and scatters at the surface and then propagates downward. This can be seen clearly in the later snapshots (3.0 s). These snapshots also show that PML2 performs well in absorbing seismic waves (Fig. 14c), while PML1 (Fig. 14b) and the sponge boundary condition (Fig. 14a) work poorly. Figures 15 and 16 show the seismograms of the horizontal and vertical components of the wavefields recorded at receivers R1 and R2 respectively, which provide further support to the conclusions drawn above.

## CONCLUSION

We presented a method that addresses irregular topography and spurious reflections at the edges of tested models simultaneously. We first incorporated the perfectly matched layer (PML) boundary condition into wave equations in Cartesian coordinates in the frequency domain and derived time-domain PML equations through inverse Fourier transformation. We then transformed the time-domain PML equations and free surface boundary conditions (FSBC) into a curvilinear coordinate system. By replacing the imaginary points in the normal second derivatives in the PML equations, we constructed a PML boundary condition with the FSBC embedded. Numerical examples show that the PML constructed in this study performs very well in attenuating spurious reflections against the sponge boundary condition, which demonstrates the correctness and effectiveness of the implemented algorithm.

## ACKNOWLEDGEMENTS

We gratefully acknowledge the department of Geosciences at the University of Tulsa, the National Natural Science Foundation of China (41404073) and the China Postdoctoral Science Foundation for their support of this research. The authors are grateful to Professor Brenton McLaury at the University of Tulsa for his help. We would also like to thank the Editor Dr. Tijmen Jan Moser, the anonymous Associate Editor and two anonymous reviewers for their constructive comments and helpful suggestions that led to significant improvements of this paper.

## REFERENCES

- Altermann Z. and Karal F. 1968. Propagation of elastic waves in layered media by finite difference methods. *Bulletin of the Seismological Society of America* 58, 367–398.
- Altermann Z. and Rotenberg A. 1969. Seismic waves in a quarter plane. *Bulletin of the Seismological Society of America* 59, 347–368.
- Appelo D. and Petersson N. 2009. A stable finite-difference method for the elastic wave equation on complex geometries with free surfaces. *Communications in Computational Physics* 5, 84–107.
- Berenger J.P. 1994. A perfectly matched layer for the absorption of electromagnetic waves. *Journal of computational physics* 114, 185–200.
- Cerjan C., Kosloff D., Kosloff R. and Reshef M. 1985. A non-reflecting boundary condition for discrete acoustic and elastic wave equations. *Geophysics* 50, 705–708.
- Chen J. 2011. Application of the nearly perfectly matched layer for seismic wave propagation in 2D homogeneous isotropic media. *Geophysical Prospecting* 59, 662–672.

- Chew W. and Liu Q. 1996. Perfectly matched layers for elastodynamics: A new absorbing boundary condition. *Journal of Computational Acoustics* **4**, 341–359.
- Clayton R. and Engquist B. 1977. Absorbing boundary conditions for acoustic and elastic wave equations. *Bulletin of the Seismological Society of America* **67**, 1529–1540.
- Collino F. and Monk P.B. 1998. Optimizing the perfectly matched layer. *Computer Methods in Applied Mechanics and Engineering* **164**(1,2), 157–171.
- Collino F. and Tsogka C. 2001. Application of the perfectly matched absorbing layer model to the linear elastodynamic problem in anisotropic heterogeneous media. *Geophysics* **66**, 294–307.
- Engquist B. and Majda A. 1977. Absorbing boundary conditions for the numerical simulation of waves. *Mathematics of Computation* **31**, 629–651.
- Fornberg B. 1988. The pseudo-spectral method: Accurate representation in elastic wave calculations. *Geophysics* **53**, 625–637.
- Guddati M.N. and Lim K.W. 2006. Continued fraction absorbing boundary conditions for convex polygonal domains. *International Journal for Numerical Methods in Engineering* **66**, 949–977.
- Hestholm S. and Ruud B. 1994. 2-D finite-difference elastic wave modeling including surface topography. *Geophysical Prospecting* **42**, 371–390.
- Hestholm S. and Ruud B. 1998. 3-D finite-difference elastic wave modeling including surface topography. *Geophysics* **63**, 613–622.
- Hvid S.L. 1994. *Three-dimensional algebraic grid generation*. PhD thesis, Technical University of Denmark.
- Jih R., McLaughlin K. and Der Z. 1988. Free-boundary conditions of arbitrary polygonal topography in a two-dimensional explicit elastic finite-difference scheme. *Geophysics* **53**, 1045–1055.
- Kantartzis N.V. 2003. Generalised higher-order FDTD-PML algorithm for enhanced analysis of 3-D waveguiding EMC structures in curvilinear coordinates. *IEEE Proceedings on Microwaves, Antennas and Propagation*, **150**(5), 351–359.
- Komatitsch D. and Martin R. 2007. An unsplit convolutional perfectly matched layer improved at grazing incidence for the seismic wave equation. *Geophysics* **72**, SM155–SM167.
- Komatitsch D. and Tromp J. 2003. A perfectly matched layer absorbing boundary condition for the second-order seismic wave equation. *Geophysical Journal International* **154**, 146–153.
- Kristek J., Moczo P. and Archuleta R.J. 2002. Efficient methods to simulate planar free surface in the 3D 4th-order staggered-grid finite-difference schemes. *Studia Geophysica et Geodaetica* **46**, 355–381.
- Lan H. and Zhang Z. 2011a. Three-dimensional wavefield simulation in heterogeneous transversely isotropic medium with irregular free surface. *Bulletin of the Seismological Society of America* **101**, 1354–1370.
- Lan H. and Zhang Z. 2011b. Comparative study of the free-surface boundary condition in two-dimensional finite-difference elastic wavefield simulation. *Journal of Geophysics and Engineering* **8**, 275–286.
- Lan H. and Zhang Z. 2012. Seismic wavefield modeling in media with fluid-filled fractures and surface topography. *Applied Geophysics* **9**, 301–312.
- Liu Y., Teng J., Lan H., Si X. and Ma X. 2014. A comparative study of finite element and spectral element methods in seismic wavefield modeling. *Geophysics* **79**(2), T91–T104.
- Lombard B., Piroux J., Gélib C. and Virieux J. 2008. Free and smooth boundaries in 2-D finite-difference schemes for transient elastic waves. *Geophysical Journal International* **172**, 252–261.
- Martin R. and Komatitsch D. 2009. An unsplit convolutional perfectly matched layer technique improved at grazing incidence for the viscoelastic wave equation. *Geophysical Journal International* **179**, 333–344.
- Mur G. 1981. Absorbing boundary conditions for the finite-difference approximation of the time-domain electromagnetic field equations. *IEEE Transactions on Electromagnetic Compatibility* **23**, 377–382.
- Rao Y. and Wang Y. 2013. Seismic waveform simulation with pseudo-orthogonal grids for irregular topographic models. *Geophysical Journal International*.
- Roden J.A. and Gedney S.D. 2000. Convolutional PML (CPML): An efficient FDTD implementation of the CFS-PML for arbitrary media. *Microwave and Optical Technology Letters* **27**, 334–339.
- Sanchez-Sesma F.J., Bravo M.A. and Herreir I. 1985. Surface motion of topographical irregularities for incident P, SV, and Rayleigh waves. *Bulletin of the Seismological Society of America* **75**, 263–269.
- Teixeira F.L. and Chew W.C. 2000. Complex space approach to perfectly matched layers: A review and some new developments. *International Journal of Numerical Modelling: Electronic Networks, Devices and Fields*, **13**(5), 441–455.
- Tian X., Kang I., Kim G. and Zhang H. 2008. An improvement in the absorbing boundary technique for numerical simulation of elastic wave propagation. *Journal of Geophysics and Engineering* **5**, 203–209.
- Wong H. 1982. Effect of surface topography on the diffraction of P, SV, and Rayleigh waves. *Bulletin of the Seismological Society of America* **72**, 1167–1183.
- Yang D., Wang S., Zhang Z. and Teng J. 2003. n-Times absorbing boundary conditions for compact finite-difference modeling of acoustic and elastic wave propagation in the 2D TI medium. *Bulletin of the seismological society of America* **93**, 2389–2401.
- Zeng Y.Q. and Liu Q.H. 2001. A staggered-grid finite-difference method with perfectly matched layers for poroelastic wave equations. *The Journal of the Acoustical Society of America* **109**, 2571–2580.
- Zhang W. and Chen X. 2006. Traction image method for irregular free surface boundaries in finite difference seismic wave simulation. *Geophysical Journal International* **167**, 337–353.
- Zheng Y. and Huang X. 2002. Anisotropic perfectly matched layers for elastic waves in Cartesian and curvilinear coordinates. *MIT Report*, 77843–73368. URI: <http://hdl.handle.net/1721.1/67857>